

# Planar $\text{CH}_3\text{NH}_3\text{PbI}_3$ Perovskite Solar Cells with Constant 17.2% Average Power Conversion Efficiency Irrespective of the Scan Rate

Jin Hyuck Heo, Dae Ho Song, Hye Ji Han, Seong Yeon Kim, Jun Ho Kim, Dasom Kim, Hee Won Shin, Tae Kyu Ahn, Christoph Wolf, Tae-Woo Lee, and Sang Hyuk Im\*

Since Kojima et al.<sup>[1]</sup> reported  $\text{CH}_3\text{NH}_3\text{PbX}_3$  ( $\text{MAPbX}_3$ ,  $X = \text{Br}, \text{I}$ ) perovskite-sensitized solar cells, the perovskite hybrid solar cells have been of great interest because of their unique properties such as long charge carrier's diffusion length, strong light absorptivity, ambipolar charge transport, high open circuit voltage, and solution processibility. The perovskite hybrid solar cells can be roughly classified to mesoscopic,<sup>[2]</sup> meso-superstructured,<sup>[3]</sup> and planar type.<sup>[4]</sup> The first uses the mesoscopic  $\text{TiO}_2$  electron conductor which can tune the electron flux coming from the hybrid perovskite light absorber. Generally, pure or alloyed perovskite hybrid solar cells adopt this device architecture because the electrons generated in perovskite are injected into mesoscopic  $\text{TiO}_2$ . Meanwhile, the second uses the mesoscopic insulator such as  $\text{Al}_2\text{O}_3$  and as a result, the electrons are transported to electrode through the perovskite itself because the electron injection from perovskite into  $\text{Al}_2\text{O}_3$  is blocked. The mixed halide perovskites such as  $\text{MAPbI}_{3-x}\text{Cl}_x$  ( $x = 0.01\text{--}0.03$ ) are usually chosen for this device structure. The last utilizes the dense thin electron conducting layer such as  $\text{TiO}_2$ ,  $\text{ZnO}$ , PCBM ([6,6]-phenyl- $\text{C}_{61}$ -butyric acid methyl ester) instead of mesoscopic  $\text{TiO}_2$ , of which the electrons generated in planar perovskite thin film are injected into the electron conductor. All of pure, alloyed, and mixed halide perovskites can be used for this planar type of perovskite hybrid solar cell.

Although the record efficiency of perovskite hybrid solar cells reached up to 20.1%,<sup>[5]</sup> it was known that the perovskite hybrid solar cells often exhibited significant hysteresis of  $J$ - $V$

(photocurrent density–voltage) curves with respect to the scan direction due to the charge accumulation or dielectric polarization by ferroelectric properties of perovskite materials.<sup>[6,7]</sup> It is quite important issue to reduce the  $J$ - $V$  hysteresis with the scan direction in order to determine the real device efficiency. Jeon et al.<sup>[2h]</sup> reported that the 200–300-nm thick mesoscopic  $\text{TiO}_2$  layer is necessary to reduce  $J$ - $V$  hysteresis with respect to scan direction because the electron–hole diffusion lengths are corresponded to 100–200 nm and the mesoscopic  $\text{TiO}_2$  electrode can adjust the flux of electrons ( $J_e$ ) due to its controlled interface area.<sup>[2h]</sup> In solar cell, the highest device efficiency is obtained when the electron flux ( $J_e$ ) and the hole flux ( $J_h$ ) is balanced, of which the flux stands for the number of charge carriers per unit area and time. Otherwise, the unbalanced charge carriers should be recombined by the direct recombination of electrons and holes or the retarded recombination of charge carriers due to the trapping at trap sites. If the material is 100% pure without any traps, the unbalanced charge carriers should be recombined by direct recombination such as radiative or nonradiative decay. Therefore, the traps are closely related to the response time of solar cells and the mesoscopic cells might have advantage to balance the  $J_e$  and  $J_h$  due to the controllable interface area than the planar cells. This means that the unbalance of  $J_e$  and  $J_h$  leads charge accumulation to traps and the accumulated charge carriers at traps make  $J$ - $V$  hysteresis with respect to the scan direction. In mesoscopic  $\text{TiO}_2/\text{MAPbI}_3$  perovskite hybrid solar cells, the major surface traps might be located at mesoscopic  $\text{TiO}_2/\text{MAPbI}_3$  interface due to many junctions between  $\text{TiO}_2$  nanocrystals. Therefore, we should consider both interface area and number of surface traps to minimize  $J$ - $V$  hysteresis. So many junctions by thick mesoscopic  $\text{TiO}_2$  is good for increasing  $J_e$  but is bad for reducing  $J$ - $V$  hysteresis due to increased surface traps.

On the other hand, although the planar perovskite hybrid solar cells have the simplest device architecture like bilayer organic solar cells and the low temperature solution process is possible due to the absent of mesoscopic  $\text{TiO}_2$  electrode which generally requires hot processing temperature, it often suffers from the severe  $J$ - $V$  hysteresis with respect to the scan direction. For instance, recently Zhou et al.<sup>[4i]</sup> achieved 19.3% planar  $\text{MAPbI}_{3-x}\text{Cl}_x$  mixed halide perovskite hybrid solar cells via spin-coating method under controlled humid atmosphere. However, it revealed significant  $J$ - $V$  hysteresis with respect to the forward and reverse scan direction. Accordingly, it is difficult to exactly determine the power conversion efficiency of planar perovskite hybrid solar cells. It is also known that the formation of perovskite hybrid thin film with full surface coverage on

J. H. Heo, D. H. Song, H. J. Han, Prof. S. H. Im  
Functional Crystallization Center (FCC)  
Department of Chemical Engineering  
Kyung Hee University  
1732 Deogyong-daero, Giheung-gu, Yongin-si,  
Gyeonggi-do 446-701, Republic of Korea  
E-mail: imromy@khu.ac.kr



S. Y. Kim, Prof. J. H. Kim  
Department of Physics  
Incheon National University  
119 Academy-ro, Yeonsu-gu, Incheon 406-772, Republic of Korea  
D. Kim, Dr. H. W. Shin, Prof. T. K. Ahn  
Department of Energy Science  
Sungkyunkwan University  
Seobu-ro 2066, Jangan-gu, Suwon 440-746, Republic of Korea  
C. Wolf, Prof. T.-W. Lee  
Department of Materials Science and Engineering  
Pohang University of Science and Technology (POSTECH)  
77 Cheongam-Ro, Nam-Gu, Pohang,  
Gyungbuk 790-784, Republic of Korea

DOI: 10.1002/adma.201500048

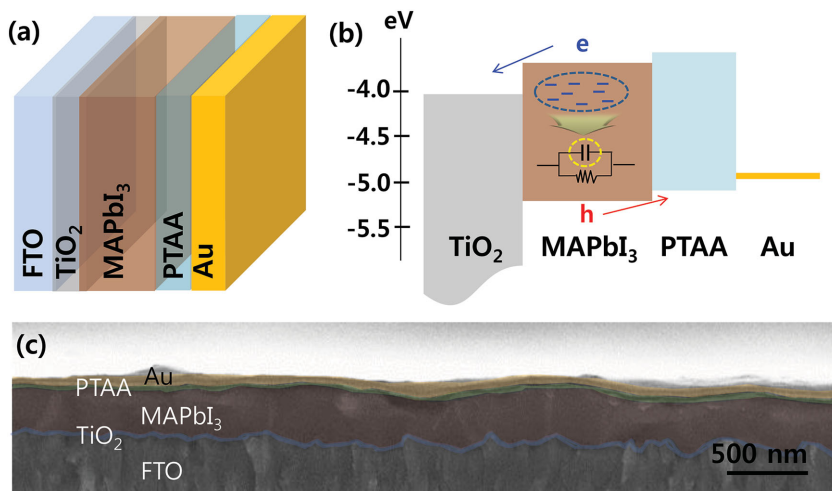


**Figure 1.** a) Schematic illustration of planar MAPbI<sub>3</sub> perovskite hybrid solar cell, b) its band energy diagram, and c) the SEM cross-sectional image of representative device.

the electron conductor/FTO (F doped SnO<sub>2</sub>) substrate is tricky. Here, we report on the straightforward method for the formation of highly pure perovskite thin film with full surface coverage thereby not only reducing significantly the *J*–*V* hysteresis of perovskite hybrid solar cells with respect to the scan direction but also demonstrating the 17.2% planar CH<sub>3</sub>NH<sub>3</sub>PbI<sub>3</sub> perovskite solar cells with constant average power conversion efficiency irrespective with the scan rate.

**Figure 1a** depicts the device structure comprised FTO/dense TiO<sub>2</sub> electron conductor (≈50 nm)/MAPbI<sub>3</sub> perovskite (≈300 nm)/PTAA (≈40 nm)/Au. In a typical process for the fabrication of the perovskite hybrid device, a dense TiO<sub>2</sub> electron conductor of ≈50 nm in thickness was deposited on a FTO glass by the spray pyrolysis deposition method. The pinhole-free MAPbI<sub>3</sub> thin films were deposited on the TiO<sub>2</sub>/FTO substrate by spin-coating of 40 wt% MAPbI<sub>3</sub>/DMF (*N,N*-dimethylformamide: 1 mL) with 100 μL HI or 40 wt% MAPbI<sub>3</sub>/DMSO (dimethyl sulfoxide: 1 mL) solutions at 3000 rpm for 200 s. Then, the PTAA solution was spin-coated on MAPbI<sub>3</sub>/TiO<sub>2</sub>/FTO substrate at 3000 rpm for 30 s. Finally, the Au counter electrode was deposited by thermal evaporation. The representative SEM cross-sectional image of planar MAPbI<sub>3</sub> perovskite hybrid solar cell was shown in Figure 1c.

Upon illumination of light, the MAPbI<sub>3</sub> perovskite generates electron–hole pairs and the electrons (holes) are then transported into TiO<sub>2</sub> electron conductor (PTAA hole conductor) as shown in Figure 1b. If the MAPbI<sub>3</sub> perovskite layer has some defects, the photocurrent response will be delayed by the internal trap states because the traps act as internal capacitance due to the trap filling and trapping/detrapping process.<sup>[8]</sup> Therefore, the impurities in MAPbI<sub>3</sub> perovskite layer will retard the charge injection from MAPbI<sub>3</sub> into TiO<sub>2</sub>. In addition, the capacitance element in the impure MAPbI<sub>3</sub> will make severe *J*–*V* hysteresis with respect to scan direction. Especially, the planar MAPbI<sub>3</sub> perovskite hybrid solar cells are expected to reveal more severe *J*–*V* hysteresis than the mesoscopic MAPbI<sub>3</sub> perovskite solar cells<sup>[9,10]</sup> because the mesoscopic TiO<sub>2</sub> electron conductor can compensate the electron flux due to the large surface area even though the electron injection is retarded by

the traps whereas the planar TiO<sub>2</sub> electron conductor cannot. The balanced electron and hole flux will not create charge accumulation within MAPbI<sub>3</sub> perovskite layer if the charge transport is not significantly hindered in the electron conductor or the hole conductor. Accordingly, it will be crucial to form pure MAPbI<sub>3</sub> perovskite layer in order to reduce the *J*–*V* hysteresis with respect to scan direction in the planar MAPbI<sub>3</sub> perovskite hybrid solar cells.

As a model system for the formation of pinhole-free MAPbI<sub>3</sub> perovskite thin film on TiO<sub>2</sub>/FTO substrate via single step spin-coating process, we used 40 wt% MAPbI<sub>3</sub>/DMSO (1 mL) solution and 40 wt% MAPbI<sub>3</sub>/DMF (1 mL) solution with 100 μL HI additive solution, respectively, because the DMSO solvent and DMF solvent with HI additive have better solubility to MAPbI<sub>3</sub> perovskite

than the pure DMF solvent thereby facilitating the formation of pinhole-free thin film.<sup>[2b,4d]</sup> During a spin-coating process, a MAPbI<sub>3</sub> perovskite solution are spread on the TiO<sub>2</sub>/FTO substrate by centrifugal force and the MAPbI<sub>3</sub> perovskite is crystallized on the substrate from the periphery to the center of the substrate by further evaporation of solvent.<sup>[4d]</sup> At the moment, more concentrated MAPbI<sub>3</sub> perovskite solution in DMSO and DMF with HI additive can form more dense MAPbI<sub>3</sub> thin film on the whole surface of TiO<sub>2</sub>/FTO substrate due to the increased solubility. **Figure 2a,b** shows the SEM surface images of MAPbI<sub>3</sub> perovskite thin film deposited on TiO<sub>2</sub>/FTO substrate via simple one-step spin-coating process with MAPbI<sub>3</sub>/DMSO (1 mL) solution and MAPbI<sub>3</sub>/DMF (1 mL) solution with 100 μL HI additive solution. The SEM images clearly confirm the formation of dense MAPbI<sub>3</sub> thin film without pinholes. To compare the crystalline morphology of whole surface of DMSO- and HI-MAPbI<sub>3</sub> film, we checked SEM surface images of them in detail as shown in Figure S1, Supporting Information. We found that the DMSO-MAPbI<sub>3</sub> film has very large crystalline domains, whereas the HI-MAPbI<sub>3</sub> film has not any crystalline domains. Their corresponding SEM cross-sectional images in Figure 2c,d indicate that the thickness of both MAPbI<sub>3</sub> layers is ≈300 nm. To check the purity of MAPbI<sub>3</sub> perovskite layer formed by MAPbI<sub>3</sub>/DMSO solution (DMSO-MAPbI<sub>3</sub>) and MAPbI<sub>3</sub>/DMF solution with HI additive solution (HI-MAPbI<sub>3</sub>), the XRD patterns were shown in Figure 2e. The XRD patterns clearly indicate that the MAPbI<sub>3</sub> perovskite film formed by MAPbI<sub>3</sub>/DMSO solution has some impurities such as PbI<sub>2</sub> whereas no impurities are detectable in MAPbI<sub>3</sub> film formed by MAPbI<sub>3</sub>/DMF solution with HI additive. Although Jeon et al.<sup>[2b]</sup> reported that the DMSO additive does not deteriorate the purity of MAPbI<sub>3</sub> by nonsolvent dripping process, tiny PbI<sub>2</sub> impurity peaks always existed in the closer look of XRD patterns. Similarly, the MAPbI<sub>3</sub> crystals formed by in MAPbI<sub>3</sub>/DMF solution (DMF-MAPbI<sub>3</sub>) revealed also small amount of PbI<sub>2</sub> impurity peaks in Figure 2e. The formation of impurities in MAPbI<sub>3</sub> film formed by the conventional MAPbI<sub>3</sub>/DMF and MAPbI<sub>3</sub>/DMSO solutions might be associated with the fact that practically, it is very difficult to exactly mix equimolar concentration of MAI and PbI<sub>2</sub> or the MAI can be decomposed or

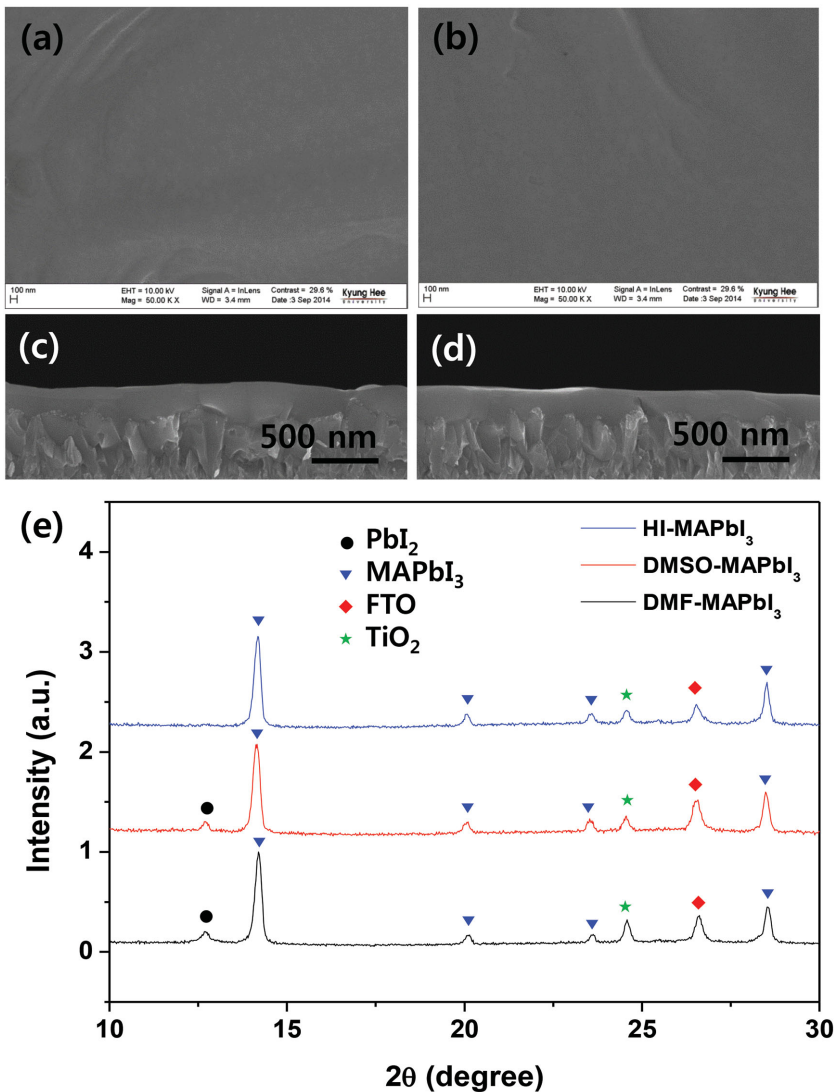


**Figure 2.** SEM surface a,b) and cross-sectional c,d) images of MAPbI<sub>3</sub> perovskite thin films prepared by one-step spin-coating process using MAPbI<sub>3</sub>/DMSO solution (DMSO-MAPbI<sub>3</sub>: (a) and (c)) and MAPbI<sub>3</sub>/DMF solution with HI additive solution (HI-MAPbI<sub>3</sub>: (b) and (d)); and e) XRD patterns of MAPbI<sub>3</sub> perovskite thin films (DMF-MAPbI<sub>3</sub> = MAPbI<sub>3</sub>/DMF solution without HI additive solution).

sublimated during the formation of MAPbI<sub>3</sub> crystal film. Therefore, the mesoscopic MAPbI<sub>3</sub> perovskite solar cells exhibited small hysteresis of short circuit current density ( $J_{sc}$ ), open circuit voltage ( $V_{oc}$ ), fill factor (F.F.), and efficiency even though the thickness of mesoscopic TiO<sub>2</sub> is optimized.<sup>[2h]</sup> On the other hand, the added HI solution can reduce the formation of PbI<sub>2</sub> impurities by decomposition of MAI from MAPbI<sub>3</sub> because the HI solution can recover the methylamine (decomposed product of MAI) into MAI thereby significantly suppressing the decomposition reaction of MAPbI<sub>3</sub> perovskite. Accordingly, it is expected that the planar MAPbI<sub>3</sub> perovskite hybrid solar cells with high purity will exhibit smaller  $J$ - $V$  hysteresis with respect to scan direction and scan rate. The effect of PbI<sub>2</sub> impurity on the  $J$ - $V$  hysteresis with respect to the scan direction is demonstrated in Figure S2, Supporting Information.

Figure 3a is UV-vis absorption spectra of FTO/TiO<sub>2</sub>/MAPbI<sub>3</sub> films prepared from DMSO-MAPbI<sub>3</sub> and HI-MAPbI<sub>3</sub> solutions indicating that both MAPbI<sub>3</sub> films have similar light harvesting efficiency due to the same thickness of MAPbI<sub>3</sub> layer (see Figure 2c,d). Figure 3b exhibits the representative  $J$ - $V$  curves of planar MAPbI<sub>3</sub> perovskite hybrid solar cells prepared by DMSO-MAPbI<sub>3</sub> and HI-MAPbI<sub>3</sub> solutions with respect to scan direction under 200 ms of delay time and 10 mV per point (voltage scan step) condition. As expected from the XRD analysis, the planar MAPbI<sub>3</sub> perovskite hybrid solar cells prepared by DMSO-MAPbI<sub>3</sub> had more serious  $J$ - $V$  hysteresis with respect to the scan direction than the cell by HI-MAPbI<sub>3</sub> solutions. The photovoltaic properties of DMSO-MAPbI<sub>3</sub> (DMSO) and HI-MAPbI<sub>3</sub> (HI) planar perovskite hybrid solar cells were listed in Table 1. The DMSO-MAPbI<sub>3</sub> device exhibited that 1.06 V of  $V_{oc}$ , 18.7 mA cm<sup>-2</sup> of  $J_{sc}$ , 59% of F.F., and 11.7% of power conversion efficiency ( $\eta$ ) at forward scan direction at 1 sun condition and 1.08 V of  $V_{oc}$ , 18.9 mA cm<sup>-2</sup> of  $J_{sc}$ , 70% of F.F., and 14.3% of  $\eta$  at backward scan direction thereby yielding to 13% of average power conversion efficiency ( $\eta_{avg}$ ). On the other hand, the HI-MAPbI<sub>3</sub> device exhibited 1.1 V of  $V_{oc}$ , 20.4 mA cm<sup>-2</sup> of  $J_{sc}$ , 75% of F.F., and 16.8% of  $\eta$  at forward scan direction and 1.1 V of  $V_{oc}$ , 20.5 mA cm<sup>-2</sup> of  $J_{sc}$ , 78% of F.F., and 17.6% of  $\eta$  at backward scan direction, thereby yielding to 17.2% of  $\eta_{avg}$ . These results indicate that the pure MAPbI<sub>3</sub> perovskite can reduce the  $J$ - $V$  hysteresis with respect to scan direction and increase the average power conversion efficiency as well. The improved efficiency might be attributed to the enhanced charge injection and/or charge collection efficiency because the HI-MAPbI<sub>3</sub> hybrid solar cells exhibited better EQE (external quantum efficiency) spectrum than the DMSO-MAPbI<sub>3</sub> cells as shown in Figure 3a. The photovoltaic parameters of DMSO-MAPbI<sub>3</sub> and HI-MAPbI<sub>3</sub> planar hybrid solar cells with respect to scan direction under different delay time conditions were summarized in Table S1, Supporting Information. The power conversion efficiencies of DMSO-MAPbI<sub>3</sub> and HI-MAPbI<sub>3</sub> planar hybrid solar cells with respect to scan direction at different delay time condition were plotted in Figure 3c. This clearly shows that the  $J$ - $V$  hysteresis of HI-MAPbI<sub>3</sub> planar hybrid solar cells with respect to scan direction is significantly reduced. The HI-MAPbI<sub>3</sub> planar hybrid solar cells had the coincidence of power conversion efficiencies measured by forward and backward scan condition over 500 ms of delay time whereas the DMSO-MAPbI<sub>3</sub> cells had over 1000 ms of delay time. It should be noted that the HI-MAPbI<sub>3</sub> planar hybrid solar cells exhibited constant  $\eta_{avg}$

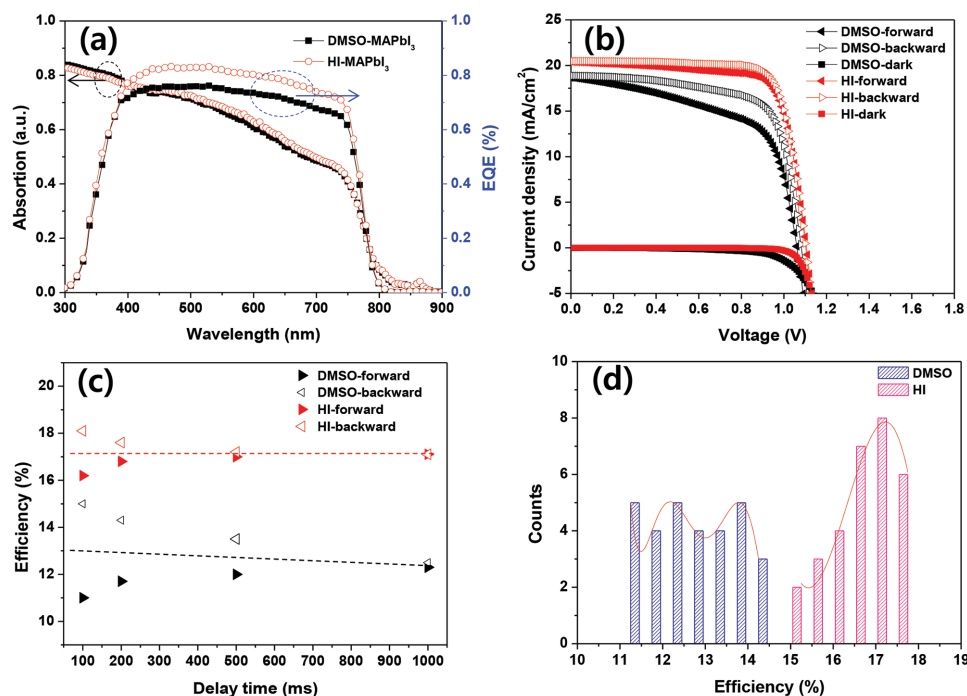


**Figure 3.** a) Absorption and EQE (external quantum efficiency) spectra of DMSO-MAPbI<sub>3</sub> and HI-MAPbI<sub>3</sub> film and device, respectively and b) *J*-*V* curves, c) forward and backward efficiency with delay time, and d) efficiency deviation of DMSO-MAPbI<sub>3</sub> and HI-MAPbI<sub>3</sub> perovskite hybrid solar cells. (DMSO = DMSO-MAPbI<sub>3</sub> device, HI = HI-MAPbI<sub>3</sub> device, forward = forward scan, backward = backward scan.)

irrespective to the delay time whereas the DMSO-MAPbI<sub>3</sub> cells showed slightly declining  $\eta_{\text{avg}}$  with the delay time. Figure 3d is the  $\eta_{\text{avg}}$  deviation of different 30 DMSO-MAPbI<sub>3</sub> and HI-MAPbI<sub>3</sub> hybrid solar cells, respectively, indicating that the  $\eta_{\text{avg}}$  is significantly improved by introduction HI additive which enables to form pure MAPbI<sub>3</sub> perovskite thin film by simple one-step spin-coating process. It is also noted that the existence of *J*-*V* hysteresis with respect to the scan direction and scan rate do not make serious problem if we measure correctly measure the efficiency of perovskite hybrid solar cells through sufficiently increasing the delay time (>1000 ms) where the *J*-*V* curves of forward and backward scan condition are coincided. Hence, we need to carefully check the *J*-*V* curves in perovskite hybrid solar cells to exactly determine the real efficiency. The current density under applied optimal bias voltage at maximum power point with light soaking time shown in Figure S3, Supporting Information, clearly confirms that the HI-MAPbI<sub>3</sub> hybrid solar cell has a constant power conversion efficiency under continuous light illumination of 1 sun, whereas the

DMSO-MAPbI<sub>3</sub> solar cell's efficiency is slightly declined with light soaking time.

To understand the effect of HI additive on the device efficiency and *J*-*V* hysteresis due to the higher impurities which might be associated with the traps, the trap density of completed solar cell was investigated by using admittance spectroscopy (AS). AS can probe trap energy level and trap density of the absorber layer.<sup>[11]</sup> The trap energy level is derived by the relation,  $\omega_0 = \beta T^2 \exp\left(\frac{-E_a}{k_B T}\right)$ , where  $\omega_0$  is characteristic transi-

tion frequency,  $\beta$  is temperature independent parameter,  $E_a$  is depth of trap energy level,  $k_B$  is the Boltzmann constant, and  $T$  is the temperature. Using this equation, Arrhenius plot of characteristic frequency is plotted, and  $E_a$  is the slope of the Arrhenius plot line. The trap density can be derived by the equation,

$$N_t = -\frac{V_{\text{bi}}}{qw} \frac{dC}{d\omega} \frac{\omega}{k_B T}$$

frequency,  $q$  is the elementary charge,  $k_B$  is the Boltzmann constant,  $T$  is the temperature,  $V_{\text{bi}}$  is the built-in potential, and  $w$  is the depletion width, respectively. The values of  $V_{\text{bi}}$  and  $w$  are obtained from Mott-Schottky analysis.

Figure 4a-f shows the results of AS measurements. DMSO solar cell shows trap energy level of 0.27 eV and trap energy density of  $\approx 10^{17} \text{ cm}^{-3}$ , whereas HI solar cell exhibits trap energy level of 0.28 eV and trap energy density of  $\approx 10^{16} \text{ cm}^{-3}$ . The trap energy of 0.27–0.28 eV is shallower than that reported by Shao et al.<sup>[12]</sup> and deeper than the result by Duan et al.<sup>[13]</sup> It should be noted that trap density of DMSO cell is 10 times larger than that of HI cell. The higher defect density induces larger electrical element of capacitance in the

**Table 1.** Photovoltaic properties of DMSO-MAPbI<sub>3</sub> (DMSO) and HI-MAPbI<sub>3</sub> (HI) planar perovskite hybrid solar cells (100 mW cm<sup>-2</sup> AM 1.5G, delay time = 200 ms, voltage scan step = 10 mV).

Device	Scan direction	$V_{\text{oc}}$ [V]	$J_{\text{sc}}$ [mA cm <sup>-2</sup> ]	F.F. [%]	$\eta$ [%]	Avg. $\eta$ [%]
DMSO	Forward	1.06	18.7	59	11.7	13.0
	Backward	1.08	18.9	70	14.3	
HI	Forward	1.1	20.4	75	16.8	17.2
	Backward	1.1	20.5	78	17.6	

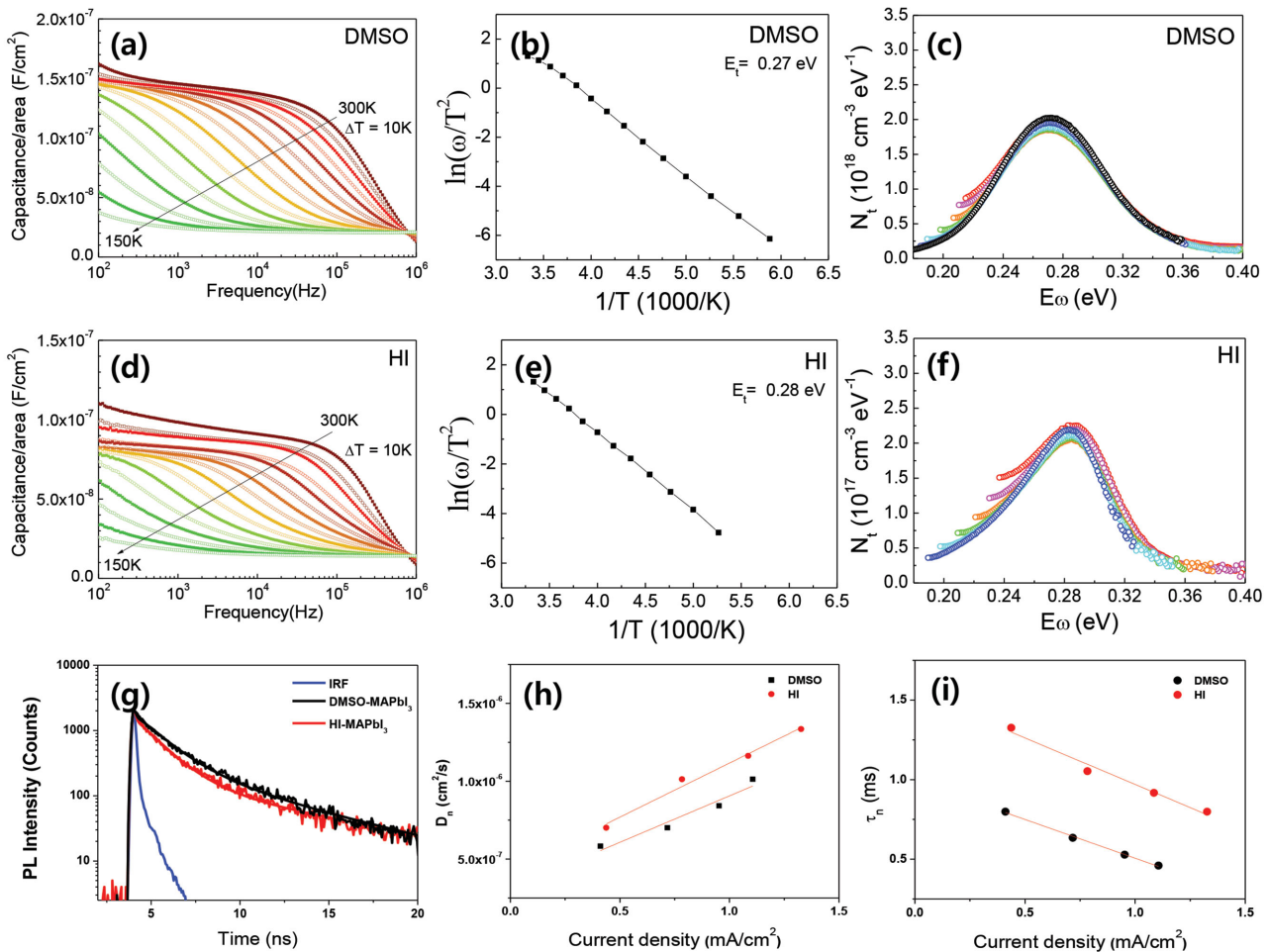


**Figure 4.** Temperature dependent capacitance spectra (a) for DMSO, d) for HI, Arrhenius plots of characteristic frequencies (b) for DMSO, e) for HI, and trap density profiles (c) for DMSO, f) for HI of DMSO (a–c) and HI (d–f) cells, respectively; g) time-resolved photoluminescent (PL) decay curves of DMSO and HI; and h,i) charge carrier's diffusion coefficient from (h) IMPS and decay time from (i) IMVS of DMSO and HI device. (DMSO = DMSO-MAPbI<sub>3</sub> planar hybrid solar cell, HI = HI-MAPbI<sub>3</sub> planar hybrid solar cell.)

complete solar cell, which may result in hysteresis of solar cell. It should be noted that the capacitance elements are attributed to the impurities in MAPbI<sub>3</sub> perovskite thin film within itself because the charges can be accumulated at the trap sites. Therefore, the traps are gradually filled at forward scan condition, whereas the traps are fully filled at backward scan condition. Under fast scan rate (short delay time) condition of  $J-V$  curves, the photocurrent is measured before reaching the saturation value so that the  $J_{sc}$  is increased with the delay time at forward scan condition, whereas the  $J_{sc}$  is decreased with the delay time due to the recombination through the trap sites at backward scan condition. As a result, the  $\eta$  of DMSO-MAPbI<sub>3</sub> device reveals significant hysteresis with respect to the scan direction, whereas the  $J_{sc}$  of HI-MAPbI<sub>3</sub> device is less sensitive with the scan rate than the DMSO-MAPbI<sub>3</sub> device. Consequently, the HI-MAPbI<sub>3</sub> perovskite hybrid solar cells exhibited constant  $\eta_{avg}$  irrespective to the scan rate meanwhile the  $\eta_{avg}$  of DMSO-MAPbI<sub>3</sub> device was slightly decreasing with the delay time. In addition, we need to consider the change of ferroelectric properties with different perovskite

thin films of DMSO-MAPbI<sub>3</sub> and HI-MAPbI<sub>3</sub>. If the change of dielectric polarization by ferroelectric properties is dominant factor to make  $J-V$  hysteresis, the  $J-V$  hysteresis were greatly dependent on the perovskite crystalline domain size but here the morphologies of perovskite thin films were similar so that **the traps might be the major factor to make  $J-V$  hysteresis** (see the more detailed explanation for AS analysis in the Supporting Information).

To compare the charge carrier dynamics (charge transfer or charge injection/separation behavior), we measured the time-resolved photoluminescent (PL) decay curves of DMSO-MAPbI<sub>3</sub> and HI-MAPbI<sub>3</sub> planar hybrid solar cells as shown in Figure 4g.<sup>[14]</sup> **The shortened PL decay in HI-MAPbI<sub>3</sub> solar cells confirmed the faster transfer of the charge carriers** into TiO<sub>2</sub> electron conductor and PTAA hole conductor than that in the DMSO-MAPbI<sub>3</sub> solar cells, **which means that HI-MAPbI<sub>3</sub> perovskite hybrid solar cells can inject the charge carriers from MAPbI<sub>3</sub> perovskite into TiO<sub>2</sub> electron conductor more efficiently.** From the convolution of the time-resolved PL decays with a biexponential function, **the average**

PL lifetime ( $\tau_{\text{avg}}$ ) of HI-MAPbI<sub>3</sub> (2.058 ns) is shorter than that of DMSO-MAPbI<sub>3</sub> (2.278 ns), as listed in Table S2, Supporting Information.

To check what the purity of MAPbI<sub>3</sub> perovskite can affect the device operation, we measured diffusion coefficient ( $D_n$ ) and charge carrier's life time ( $\tau_n$ ) from IMPS (intensity modulated photocurrent spectroscopy) and IMVS (intensity modulated photovoltage spectroscopy) analysis as shown in Figure 4h,i. The original Nyquist plots of IMPS and IMVS were shown in Figure S4, Supporting Information. From the plots of  $D_n$  and  $\tau_n$  with current density ( $J$ ), we could recognize that the  $D_n$  and  $\tau_n$  of HI-MAPbI<sub>3</sub> planar hybrid solar cells are increased to  $\approx 1.3$  and  $\approx 1.6$ -fold, respectively, than the DMSO-MAPbI<sub>3</sub> devices. Accordingly, the diffusion length ( $L_n = (D_n \cdot \tau_n)^{0.5}$ ) of MAPbI<sub>3</sub> planar hybrid solar cells was increased from  $\approx 230$  to  $\approx 350$  nm by using pure MAPbI<sub>3</sub> perovskite (HI-MAPbI<sub>3</sub>). From the analysis of transient PL decay, IMPS, and IMVS, we could conclude that i) the EQE of HI-MAPbI<sub>3</sub> planar hybrid solar cell is improved by the enhanced charge injection/separation efficiency and charge collection efficiency thereby improving  $J_{\text{sc}}$ ; ii) the F.F. and  $V_{\text{oc}}$  of HI-MAPbI<sub>3</sub> planar hybrid solar cell is enhanced by the improved  $D_n$  and  $\tau_n$  thereby reducing the backward recombination of electrons and holes; and iii) the  $J$ - $V$  hysteresis of HI-MAPbI<sub>3</sub> device with respect to the scan direction and rate is greatly reduced by the formation of highly pure MAPbI<sub>3</sub> perovskite by addition of HI additive solvent thereby eliminating number of traps which may create the internal capacitance elements within MAPbI<sub>3</sub> perovskite layer.

In summary, the pinhole-free MAPbI<sub>3</sub> perovskite hybrid thin-films were formed by the simple one-step spin-coating process by using MAPbI<sub>3</sub>/DMSO solution and MAPbI<sub>3</sub>/DMF with HI additive solvent. The XRD analysis confirmed that the pure MAPbI<sub>3</sub> perovskite hybrid thin film could be formed by the contribution of HI additive solvent because HI can prohibit the decomposition of MAPbI<sub>3</sub> to MAI and PbI<sub>2</sub> whereas conventional MAPbI<sub>3</sub> in DMF or DMSO solution made some impurity such as PbI<sub>2</sub>. Through the formation of pure MAPbI<sub>3</sub> perovskite hybrid thin films by introduction of HI additive solvent, we could enhance 1.3-fold of the  $\eta_{\text{avg}}$  under illumination of 1 sun (100 mW cm<sup>-2</sup> AM 1.5G) light and consequently obtained 17.2% of  $\eta_{\text{avg}}$  irrespective with the scan direction and rate because the HI-MAPbI<sub>3</sub> planar perovskite hybrid solar cells exhibited  $\approx 1.4$ -fold longer diffusion length than the DMSO-MAPbI<sub>3</sub> planar solar cells owing to  $\approx 1.3$  and  $\approx 1.6$ -fold of the improved  $D_n$  and  $\tau_n$ , respectively, than DMSO-MAPbI<sub>3</sub> planar solar cells. In addition, the charge injection/separation efficiency and trap sites are also improved by the formation of pure MAPbI<sub>3</sub> perovskite hybrid thin films. From the AS results, we found that both DMSO- and HI-cells have similar trap energy level of 0.27–0.28 eV but the HI cell has  $\approx 10$ -fold lower trap density than the DMSO cell. Therefore, the HI cell reveals lower  $J$ - $V$  hysteresis with respect to the scan direction due to the smaller number of capacitance element. Therefore, we believe that if we balance the electron ( $J_e$ ) and hole flux ( $J_h$ ) and eliminate the trap sites in MAPbI<sub>3</sub> planar perovskite hybrid solar cells, the highly efficient planar perovskite hybrid solar cells without  $J$ - $V$  hysteresis with respect to scan direction could be fabricated.

## Experimental Section

**Preparation of MAPbI<sub>3</sub> Perovskite Solution:** To synthesize CH<sub>3</sub>NH<sub>3</sub>I<sub>3</sub>, 50 mL hydriodic acid (48% in water, Aldrich) and 30 mL methylamine (40% in methanol, Junsei Chemical Co. Ltd.) were reacted in a 250-mL round-bottom flask at 0 °C for 2 h with vigorous stirring. The products were recovered by evaporation and then were dissolved in ethanol, recrystallized from diethyl ether. Finally, the products were dried at the room temperature in a vacuum oven for 24 h. To form the CH<sub>3</sub>NH<sub>3</sub>PbI<sub>3</sub> thin film, two kinds of solutions such as 40 wt% of CH<sub>3</sub>NH<sub>3</sub>PbI<sub>3</sub> in dimethyl sulfoxide and *N,N*-dimethylformamide with added 100  $\mu$ L hydriodic acid were prepared by reacting the synthesized CH<sub>3</sub>NH<sub>3</sub>I<sub>3</sub> and PbI<sub>2</sub> (Aldrich) at 1:1 mole ratio at 60 °C for 30 min.

**Device Fabrication:** To fabricate the planar CH<sub>3</sub>NH<sub>3</sub>PbI<sub>3</sub> perovskite hybrid solar cell, dense TiO<sub>2</sub> blocking layer (bl-TiO<sub>2</sub>) of  $\approx 50$  nm thickness was deposited on cleaned F-doped SnO<sub>2</sub> (FTO, Pilkington, TEC8) glass substrate by spray pyrolysis deposition (SPD) method with  $20 \times 10^{-3}$  M of titanium diisopropoxide bis(acetylacetonate) (Aldrich) solution at 450 °C. To form the CH<sub>3</sub>NH<sub>3</sub>PbI<sub>3</sub> layer on bl-TiO<sub>2</sub>/FTO substrate, the 40 wt% CH<sub>3</sub>NH<sub>3</sub>PbI<sub>3</sub> in dimethyl sulfoxide and *N,N*-dimethylformamide solution with added 100  $\mu$ L HI was then coated by spin-coating and dried on a hot plate at 100 °C for 2 min. In each solvent, the spin-coating conditions are at 2000 rpm for 60 s then 4000 rpm for 120 s and at 3000 rpm for 200 s. Poly[bis(4-phenyl)-(2,4,6-trimethylphenyl)amine] (PTAA: EM index) hole transporting materials (HTM) were spin-coated on CH<sub>3</sub>NH<sub>3</sub>PbI<sub>3</sub>/bl-TiO<sub>2</sub>/FTO substrate at 2000 rpm for 30 s by using HTM/toluene (15 mg/1 mL) with 7.5  $\mu$ L Li-bis(trifluoromethanesulfonyl) imide (Li-TFSI)/acetonitrile (170 mg/1 mL) and 7.5  $\mu$ L t-BP/acetonitrile (1 mL/1 mL) additives and without additives. Finally, Au counter electrode was deposited by thermal evaporation. The active area was fixed to 0.16 cm<sup>2</sup>. All device fabrications were conducted below 50% of relative humidity.

**Device Characterization:** The current density–voltage ( $J$ - $V$ ) curves were measured by a solar simulator (Peccell, PEC-L01) with a potentiostat (IVIUM, IviumStat) at 100 mA cm<sup>-2</sup> illumination AM 1.5G and a calibrated Si-reference cell certified by JIS (Japanese Industrial Standards). For the measurement hysteresis of  $J$ - $V$  curves, the forward and reverse scan rate was set to 200 ms/10 mV as a standard condition and was varied from 100 ms/10 mV to 1000 ms/10 mV. The  $J$ - $V$  curves of all devices were measured by masking the active area with metal mask of 0.096 cm<sup>2</sup>. The external quantum efficiency (EQE) was measured by a power source (ABET 150W Xenon lamp, 13014) with a monochromator (DONGWOO OPTORN Co., Ltd., MonoRa-500i) and a potentiostat (IVIUM, IviumStat). AS measurements were carried out by using precision LCR meter (Agilent, E4980A) under dark condition at frequencies between 0.1 and 1000 kHz. Sample was located in home-made cryostat using liquid nitrogen, and the range of measurement temperature was 150–300 K. As temperature was cooled down with cooling rate of  $\approx 2$  K min<sup>-1</sup>, capacitance spectra were measured at every 10 K, and all measurements were done at corresponding temperature with error bar of  $\pm 0.05$  K or less.

## Supporting Information

Supporting Information is available from the Wiley Online Library or from the author.

## Acknowledgements

This work was supported by the Global Frontier R&D Program of the Center for Multiscale Energy System, Mid-career Research Program (No. NRF-2013R1A2A2A01067999), and Basic Science Research Program (No. 2014R1A5A1009799) through the National Research

Foundation of Korea (NRF) funded by the Ministry of Science, ICT & Future Planning.

Received: January 5, 2015

Revised: March 31, 2015

Published online:

- [1] A. Kojima, K. Teshima, Y. Shirai, T. Miyasaka, *J. Am. Soc.* **2009**, *131*, 6050.
- [2] a) H.-S. Kim, C. R. Lee, J. H. Im, K. B. Lee, T. Moehl, A. Marchioro, S. J. Moon, R. Humphry-Baker, J. H. Yum, J. E. Moser, M. Grätzel, N.-G. Park, *Sci. Rep.* **2012**, *2*, 591; b) J. H. Heo, S. H. Im, J. H. Noh, T. N. Madal, C. S. Lim, J. A. Chang, Y. H. Lee, H.-J. Kim, A. Sarkar, Md. K. Nazeeruddin, M. Grätzel, S. I. Seok, *Nat. Photonics* **2013**, *7*, 486; c) J. H. Noh, S. H. Im, J. H. Heo, T. N. Mandal, S. I. Seok, *Nano Lett.* **2013**, *13*, 1764; d) J. H. Noh, N. J. Jeon, Y. C. Choi, Md. K. Nazeeruddin, M. Grätzel, S. I. Seok, *J. Mater. Chem. A* **2013**, *1*, 11842; e) N. J. Jeon, J. Lee, J. H. Noh, M. K. Nazeeruddin, M. Grätzel, S. I. Seok, *J. Am. Chem. Soc.* **2013**, *135*, 19087; f) J. H. Heo, S. H. Im, *Phys. Status Solidi* **2014**, *8*, 816; g) J. Burschka, N. Pellet, S. J. Moon, R. H. Baker, P. Gao, M. K. Nazeeruddin, M. Grätzel, *Nature* **2013**, *499*, 316; h) N. J. Jeon, J. H. Noh, Y. C. Kim, W. S. Yang, S. Ryu, S. I. Seok, *Nat. Mater.* **2014**, *13*, 897.
- [3] a) M. M. Lee, J. Teuscher, T. Miyasaka, T. N. Murakami, H. J. Snaith, *Science* **2012**, *338*, 643; b) J. M. Ball, M. M. Lee, A. Hey, H. J. Snaith, *Energy Environ. Sci.* **2013**, *6*, 1739; c) D. Bi, S.-J. Moon, L. Häggman, G. Boschloo, L. Yang, E. M. J. Johansson, Md. K. Nazeeruddin, M. Grätzel, *RSC Adv.* **2013**, *3*, 18762.
- [4] a) M. Liu, M. B. Johnston, H. J. Snaith, *Nature* **2013**, *501*, 395; b) O. Malinkiewicz, A. Yella, Y. H. Lee, G. M. Espallargas, M. Grätzel, M. K. Nazeeruddin, H. J. Bolink, *Nat. Photonics* **2014**, *8*, 128; c) D. Liu, T. L. Kelly, *Nat. Photonics* **2014**, *8*, 133; d) J. H. Heo, D. H. Song, S. H. Im, *Adv. Mater.* **2014**, *26*, 8179; e) Z. Xiao, Q. Dong, C. Bi, Y. Shao, Y. Yuan, J. Huang, *Adv. Mater.* **2014**, *26*, 6503; f) J.-H. Im, I.-H. Jang, N. Pellet, M. Grätzel, N.-G. Park, *Nat. Nanotechnol.* **2014**, *9*, 927; g) J. Seo, S. Park, Y. C. Kim, N. J. Jeon, J. H. Noh, S. C. Yoon, S. I. Seok, *Energy Environ. Sci.* **2014**, *7*, 2642; h) M. Xiao, F. Huang, W. Huang, Y. Dkhissi, Y. Zhu, J. Etheridge, A. Gray-Weale, U. Bach, Y.-B. Cheng, L. Spiccia, *Angew. Chem. Int. Ed.* **2014**, *126*, 10056; i) H. Zhou, Q. Chen, G. Li, S. Luo, T.-Z. Song, H.-S. Duan, Z. Hong, J. You, Y. Liu, Y. Yang, *Science* **2014**, *345*, 542.
- [5] Research Cell Efficiency Records. NREL, <http://www.nrel.gov/ncpv/> (accessed: December **2014**).
- [6] H.-S. Kim, I. Mora-Sero, V. Gonzalez-Pedro, F. Fabregat-Santiago, E. J. Juarez-Perez, N.-G. Park, J. Bisquert, *Nat. Commun.* **2013**, *4*, 2242.
- [7] J. M. Frost, K. T. Butler, F. Brivo, G. H. Hendon, M. v. Schilfgarde, A. Walsh, *Nano Lett.* **2014**, *14*, 2584.
- [8] K. Schwarzburg, F. Willig, *Appl. Phys. Lett.* **1991**, *58*, 2520.
- [9] A. Dualeh, T. Moehl, N. Tétreault, J. Teuscher, P. Gao, Md. K. Nazeeruddin, M. Grätzel, *ACS Nano* **2014**, *8*, 362.
- [10] H. J. Snaith, A. Abate, J. M. Ball, G. E. Eprron, T. Leijtens, N. K. Noel, S. D. Stranks, J. T.-W. Wang, K. Wojciechowski, W. Zhang, *J. Phys. Chem. Lett.* **2014**, *5*, 1511.
- [11] T. Walter, R. Herberholz, C. Müller, H. Schock, *J. Appl. Phys.* **1996**, *80*, 4411.
- [12] Y. Shao, Z. Xiao, C. Bi, Y. Yuan, J. Huang, *Nat. Commun.*, **2014**, *5*, 5784.
- [13] H.-S. Duan, H. Zhou, Q. Chen, P. Sun, S. Luo, T.-B. Song, B. Bob, Y. Yang, *Phys. Chem. Chem. Phys.* **2014**, *17*, 112.
- [14] S. D. Stranks, G. E. Eperon, G. Grancini, C. Menelaou, M. J. P. Alcocer, T. Leijtens, L. M. Herz, A. Petrozza, H. J. Snaith, *Science* **2013**, *342*, 344.